



Article

Design of Nanoscaled Surface Morphology of TiO₂-Ag₂O Composite Nanorods through Sputtering Decoration Process and Their Low-Concentration NO₂ Gas-Sensing Behaviors

Yuan-Chang Liang * and Yen-Chen Liu

Department of Optoelectronics and Materials Technology, National Taiwan Ocean University, Keelung 20224, Taiwan

* Correspondence: yuanvictory@gmail.com; Tel.: +886-24622192

Received: 1 August 2019; Accepted: 9 August 2019; Published: 11 August 2019



Abstract: TiO₂-Ag₂O composite nanorods with various Ag₂O configurations were synthesized by a two-step process, in which the core TiO₂ nanorods were prepared by the hydrothermal method and subsequently the Ag₂O crystals were deposited by sputtering deposition. Two types of the TiO₂-Ag₂O composite nanorods were fabricated; specifically, discrete Ag₂O particle-decorated TiO₂ composite nanorods and layered Ag₂O-encapsulated TiO₂ core-shell nanorods were designed by controlling the sputtering duration of the Ag₂O. The structural analysis revealed that the TiO₂-Ag₂O composite nanorods have high crystallinity. Moreover, precise control of the Ag₂O sputtering duration realized the dispersive decoration of the Ag₂O particles on the surfaces of the TiO₂ nanorods. By contrast, aggregation of the massive Ag₂O particles occurred with a prolonged Ag₂O sputtering duration; this engendered a layered coverage of the Ag₂O clusters on the surfaces of the TiO₂ nanorods. The TiO₂-Ag₂O composite nanorods with different Ag₂O coverage morphologies were used as chemoresistive sensors for the detection of trace amounts of NO₂ gas. The NO₂ gas-sensing performances of various TiO₂-Ag₂O composite nanorods were compared with that of pristine TiO₂ nanorods. The underlying mechanisms for the enhanced sensing performance were also discussed.

Keywords: sputtering; surface decoration; nanostructured surface; composite nanorods

1. Introduction

The development of chemosensors made from semiconductor oxides has recently become a key research topic [1,2]. Therefore, the development of highly responsive sensing oxide devices toward specific harmful gases has attracted interest in industry. For the gas sensor applications, one-dimensional (1D) metal oxides usually show better performance in comparison with their thin-film or bulk counterparts because of their high surface-to-volume ratio [3–6]. In particular, gas sensors based on 1D titanium dioxide (TiO₂) nanostructures have received considerable attention because they can be fabricated with diverse chemical and physical methods; moreover, TiO₂ has been shown to be favorable for the detection of diverse harmful gases and volatile organic vapors at elevated temperatures [5,7,8].

Recently, combining n-type oxides with p-type semiconductor oxides to form a heterogeneous structure has attracted great attention due to this combination's enhanced gas-sensing performance toward target gases [9–11]. The existence of the interfacial potential barrier at the p–n junctions of the heterogeneous structure play an important role in improving the gas-sensing performance of the constituent oxides. Several p–n junction-based sensors made from different material systems and configurations have been proposed. For examples, Woo et al. reported a discrete configuration of

p-type Cr_2O_3 nanoparticles on the surfaces of ZnO nanowires; this p–n heterostructure enhances gas selectivity and sensitivity toward trimethylamine [11]. The decoration of NiO nanoparticles in porous SnO_2 nanorods remarkably enhances the gas-sensing response to ethanol as compared with pristine SnO_2 , which can be attributed to the formation of NiO– SnO_2 p–n heterojunctions [12]. P-type Ag_2O phase-functionalized In_2O_3 nanowires shows an improved gas-sensing performance toward NO_2 gas [13]. However, reports on the incorporation of p-type oxides into n-type TiO_2 nanostructures to form a p–n junction gas sensor are limited in number.

In this study, 1D TiO_2 – Ag_2O p–n heterogeneous structures are synthesized through the combination of hydrothermal growth and sputtering methods. Ag_2O is a p-type semiconductor oxide; it has previously been used as a gas-sensing material [13]. Moreover, Ag_2O crystals with various morphologies can be synthesized through chemical or physical routes [14–16]. Notably, Ag_2O particles are mostly synthesized through chemical routes but, using such chemical routes, it is hard to control the decoration morphology of the Ag_2O crystals on 1D nanostructures [15]. By contrast, the fabrication of Ag_2O through a physical method (sputtering) is advantageous concerning the control of the Ag_2O content, crystalline quality, and coverage morphology on 1D TiO_2 . In this study, two types of TiO_2 – Ag_2O composite nanorods are synthesized. By controlling the sputtering duration of the Ag_2O , discrete Ag_2O particle-decorated TiO_2 nanorods and Ag_2O layers encapsulating TiO_2 nanorods are fabricated. The Ag_2O coverage morphology effects on the low-concentration NO_2 gas-sensing performance of the TiO_2 – Ag_2O p–n composite nanorods are systematically investigated in this study.

2. Materials and Methods

In this study, TiO_2 nanorods were grown on fluorine-doped SnO_2 (FTO) glass substrates. First, 0.25 mL of TiCl_4 and 19 mL HCl were added to 11 mL deionized water and then stirred to obtain a transparent solution for the hydrothermal growth of TiO_2 nanorods. The hydrothermal reaction was conducted at 180 °C for 3 h. For the preparation of TiO_2 – Ag_2O composite nanorods, Ag_2O crystals were decorated onto the surfaces of the TiO_2 nanorod template via sputtering. Radiofrequency magnetron sputtering of Ag_2O was conducted using a silver metallic target in an Ar/ O_2 (Ar: O_2 = 5:2) mixed ambient. The sputtering deposition temperature of the Ag_2O was maintained at 200 °C. The gas pressure during sputtering deposition was fixed at 20 mTorr and the sputtering power was fixed at 50 W for the silver target. Two sets of TiO_2 – Ag_2O composite nanorods with Ag_2O sputtering durations of 130 s and 270 s were prepared; these were represented as TiO_2 – Ag_2O -1 and TiO_2 – Ag_2O -2, respectively, in this study. The sample configurations of the TiO_2 – Ag_2O -1 and TiO_2 – Ag_2O -2 composite nanorods are shown in Figure 1.

An X-ray diffractometer (XRD; D2 PHASER, Bruker, Karlsruhe, Germany) was used to analyze the crystal structures of the TiO_2 – Ag_2O composite nanorods. Scanning electron microscopy (SEM; S-4800, Hitachi, Tokyo, Japan) and transmission electron microscopy (HRTEM; JEM-2100F, JEOL Tokyo, Japan) were used to characterize the morphology and detailed microstructures of the composite nanorod samples. The attached energy dispersive X-ray spectroscopy (EDS) of TEM was used to investigate the composition and composition distribution of the nanorod samples. Moreover, X-ray photoelectron spectroscopy (XPS; ULVAC-PHI XPS, ULVAC, Chigasaki, Japan) was used to characterize the elemental binding states of the synthesized samples.

The response of pure TiO_2 nanorods and the TiO_2 – Ag_2O nanocomposites to NO_2 was tested in a vacuum test chamber. Silver electrodes were laid on the surfaces of the samples to form electric contacts for measurements. An Agilent B2911A meter measured the resistance variation of the nanorod sensors at a constant potential of 5 V as a function of time. Constant dry air was used as the carrier gas and the desired concentration of NO_2 gas (0.5, 1.5, 3.0 ppm) was introduced into the test chamber. A direct heating approach was used to operate the sensors at elevated temperatures in the range of 200–300 °C.

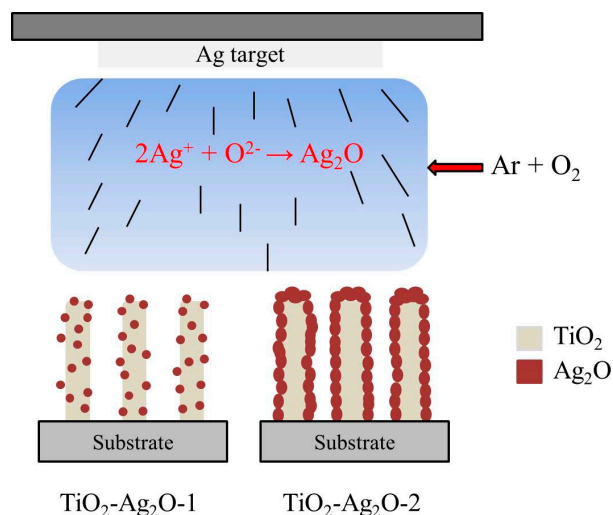


Figure 1. Sample configurations of the TiO₂-Ag₂O-1 and TiO₂-Ag₂O-2 composite nanorods synthesized with various sputtering durations of Ag₂O.

3. Results and Discussion

X-ray diffractometer (XRD) patterns of TiO₂-Ag₂O composite nanorods with various Ag₂O thin-film sputtering durations are shown in Figure 2. The distinct Bragg reflections centered at 27.46°, 36.05°, 41.22°, and 54.33° correspond to the crystallographic planes (110), (101), (111), and (211) of the rutile TiO₂ phase, respectively (JCPDS no. 00-004-0551). Moreover, the Bragg reflections centered at 32.72° and 37.98° are assigned to the crystallographic planes of cubic Ag₂O (111) and (200), respectively (JCPDS no. 00-012-0793). The XRD results reveal that highly crystalline rutile TiO₂-cubic Ag₂O composite nanorods were formed through the sputtering deposition of Ag₂O thin films onto the surfaces of the TiO₂ nanorods, and no other impurity peak was observed. As expected, the intensity of the Ag₂O Bragg reflections peaks increased with the increase of the Ag₂O thin-film sputtering duration, revealing an increased Ag₂O phase content in the composite nanorods.

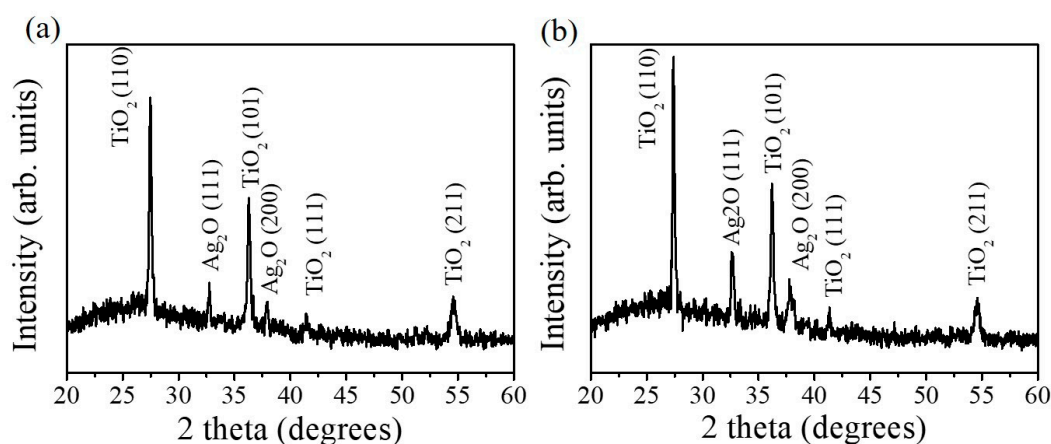


Figure 2. XRD patterns of various composite nanorods: (a) TiO₂-Ag₂O-1, (b) TiO₂-Ag₂O-2.

Figure 3a shows the scanning electron microscopy (SEM) image of the as-synthesized TiO₂ nanorods. The TiO₂ nanorods had a rectangular cross-section crystal feature with an average diameter of approximately 100 nm; the side facets of the nanorods were smooth. Figure 3b presents the SEM image of the TiO₂-Ag₂O-1 composite nanorods. The surface morphology of the composite nanorods reveals that a small amount of nanoparticle-like crystals was decorated onto the surfaces of the TiO₂ nanorods. The nanoparticle-like crystals dispersed separately on the surfaces of the TiO₂ nanorods. Figure 3c shows the SEM image of the TiO₂-Ag₂O-2 composite nanorods. The TiO₂ nanorods were homogeneously encapsulated by the aggregation of massive Ag₂O nanoparticles, resulting in the irregular-shaped cross-section crystal feature of the composite nanorods. Detailed TEM analyses were performed to further confirm the morphology change of the TiO₂-Ag₂O composite nanorods prepared at various Ag₂O sputtering durations.

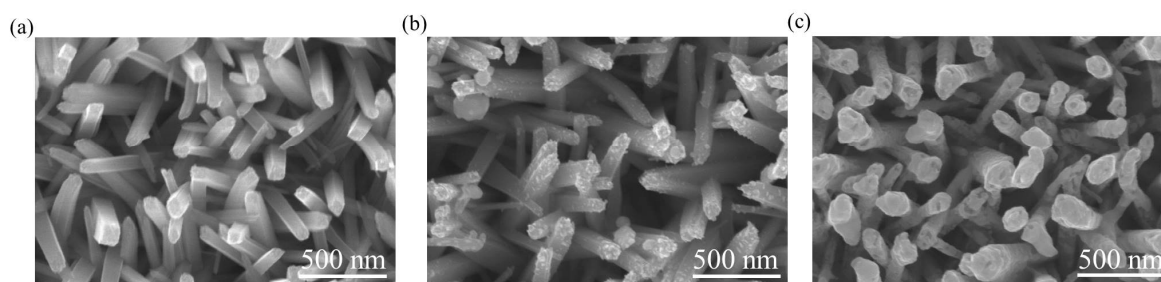


Figure 3. SEM images of various nanorods: (a) TiO₂, (b) TiO₂-Ag₂O-1, (c) TiO₂-Ag₂O-2.

Figure 4a shows the low-magnification transmission electron microscopy (TEM) image of a TiO₂-Ag₂O-1 composite nanorod. A small amount of Ag₂O particles was dispersedly decorated on the surface of the TiO₂ nanorod via the sputtering growth of the Ag₂O. The high-resolution TEM images shown in Figure 4b,c indicate distinct lattice fringes in the Ag₂O particle. Moreover, the lattice fringe distance of approximately 0.24 nm was assigned to the crystallographic plane spacing of cubic Ag₂O (200). Figure 4d exhibits the selected area electron diffraction (SAED) pattern of several TiO₂-Ag₂O-1 composite nanorods. Several clear diffraction rings associated with (111) and (200) planes of the Ag₂O and (110), (111), and (211) planes of the rutile TiO₂ were observed in the SAED pattern. This demonstrates the good crystallinity of the composite nanorods and indicates that these composite nanorods have a polycrystalline nature. Figure 4e presents the EDS spectrum of a TiO₂-Ag₂O-1 nanorod. In addition to carbon and copper signals originating from the TEM grid, Ti, Ag, and O elements were detected in the selected heterostructure and no other impurity atom was detected. The EDS elemental mapping images taken from the TiO₂-Ag₂O-1 nanorod are presented in Figure 4f. The Ti signals were homogeneously distributed over the region of the nanorod template. By contrast, the Ag signals were mainly distributed on the outer region of the composite nanorod; the distribution of Ag signals was discrete and randomly decorated on the TiO₂ surface. A good Ag₂O particle-decorated TiO₂ nanorod with a dispersive particle decoration feature was obtained in the TiO₂-Ag₂O-1 composite nanorods.

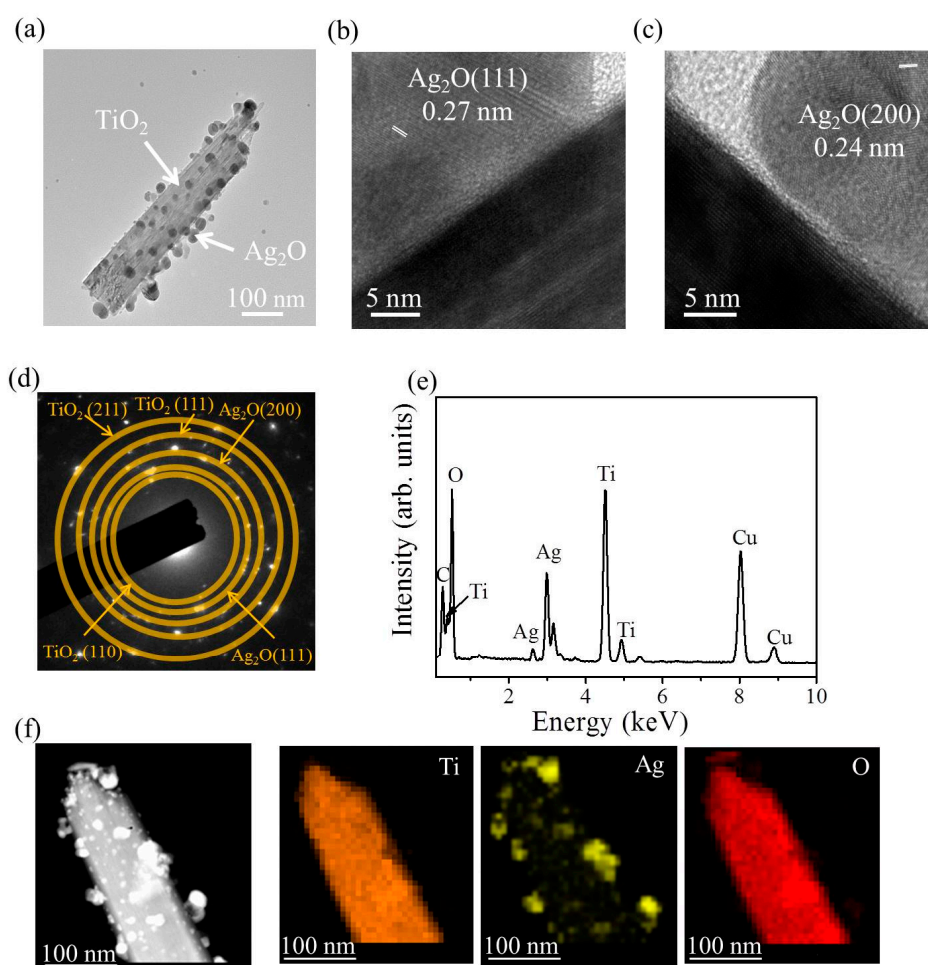


Figure 4. TEM analysis of the $\text{TiO}_2\text{-Ag}_2\text{O-1}$ composite nanorods: (a) Low-magnification TEM image of the $\text{TiO}_2\text{-Ag}_2\text{O-1}$ composite nanorod. (b,c) High-resolution TEM images taken from various regions of the composite nanorod. (d) Selected area electron diffraction (SAED) pattern of several $\text{TiO}_2\text{-Ag}_2\text{O-1}$ composite nanorods. (e) Energy dispersive X-ray spectroscopy (EDS) spectrum of the composite nanorod. (f) Ti, Ag, and O elemental mapping images taken from the selected composite nanorod.

Figure 5a shows the low-magnification TEM image of the $\text{TiO}_2\text{-Ag}_2\text{O-2}$ composite nanorod. In comparison with Figure 4a, the distribution density of the Ag_2O particles on the surface of the TiO_2 nanorod was denser and many particles were clustered, resulting in a rugged surface feature of the composite nanorod. The tiny Ag_2O particles aggregated together and fully encapsulated the surface of the TiO_2 nanorod. A clear heterointerface was observed between the TiO_2 and Ag_2O (Figure 5b,c). The distinct lattice fringes in the inner and outer regions of the composite nanorod in Figure 5b,c demonstrated a good crystallinity of the composite nanorod. The SAED pattern in Figure 5d supports the good crystallinity of the composite nanorods, as revealed in the high-resolution TEM images of the selected composite nanorod, and is also in agreement with the XRD result. Figure 5e shows the corresponding EDS spectrum of the $\text{TiO}_2\text{-Ag}_2\text{O-2}$ composite nanorod. Besides the carbon and copper signals and the elements of Ag, Ti, and O, no other impurity atom was detected from the selected composite nanorod. Notably, the relative intensity of the Ag signal was more intense than that of the $\text{TiO}_2\text{-Ag}_2\text{O-1}$ nanorod in Figure 4e, revealing a higher Ag content in $\text{TiO}_2\text{-Ag}_2\text{O-2}$ due to the prolonged sputtering duration of Ag_2O .

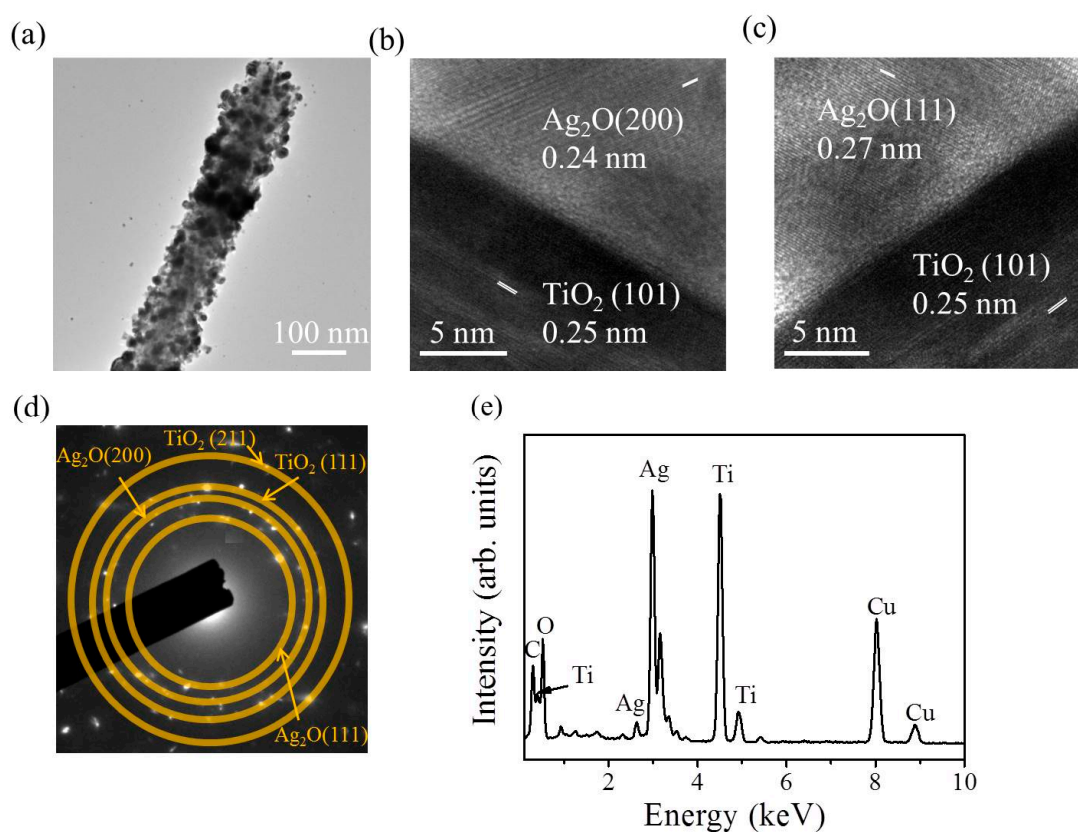


Figure 5. TEM analysis of the $\text{TiO}_2\text{-Ag}_2\text{O-2}$ composite nanorods: (a) Low-magnification TEM image of the $\text{TiO}_2\text{-Ag}_2\text{O-2}$ composite nanorod. (b,c) High-resolution TEM images taken from various regions of the composite nanorod. (d) SAED pattern of several $\text{TiO}_2\text{-Ag}_2\text{O-2}$ composite nanorods. (e) EDS spectrum of the composite nanorod.

Figure 6a shows the X-ray photoelectron spectroscopy (XPS) survey scan spectrum of the $\text{TiO}_2\text{-Ag}_2\text{O-1}$ composite nanorods. The primary features include the Ti, Ag, and O peaks that originated from the $\text{TiO}_2\text{-Ag}_2\text{O}$ composites. The trace carbon contamination on the surface of the nanorod sample originated from exposure to ambient air. No impurity atoms were detected in the nanorod sample. Figure 6b exhibits the Ag 3d core-level doublet spectrum originating from the Ag_2O decorated via sputtering; two distinct features centered at approximately 367.7 and 373.7 eV respectively correspond to the Ag 3d_{5/2} and Ag 3d_{3/2} binding energies. These binding energies are consistent with the Ag–O binding values reported for the Ag_2O phase [17]. This indicates that the silver exists in the Ag^+ valence state in the sputtered Ag_2O nanoparticles on the composite nanorods studied herein. Figure 6c displays the Ti 2p core-level doublet spectrum associated with the TiO_2 nanorod template. The distinct two features were deconvoluted into four subpeaks. The subpeaks centered at 458.7 and 464.3 eV correspond to Ti 2p_{3/2} and Ti 2p_{1/2} peaks of the Ti^{4+} valence state, respectively. By contrast, the subpeaks with a relatively weak intensity centered at 457.6 and 463.3 eV correspond to Ti 2p_{3/2} for Ti 2p_{1/2} peaks of the Ti^{3+} valence state [5]. The presence of the mixed $\text{Ti}^{4+}/\text{Ti}^{3+}$ valence state indicates the possible presence of oxygen vacancies in the surfaces of the as-synthesized TiO_2 nanorods [5,8]. The O1s spectrum of the composite nanorods is shown in Figure 6d. The asymmetric O1s spectrum was deconvoluted into three subpeaks centered at 532.5, 531.2, and 529.2 eV. Notably, the subpeaks centered at 529.2 and 531.2 eV are ascribed to the lattice oxygen in Ag_2O and TiO_2 , respectively [18,19]. Moreover, the external adsorbed –OH groups or water molecules on the surfaces of the composite nanorods are reflected by a subpeak at approximately 532.5 eV [20].

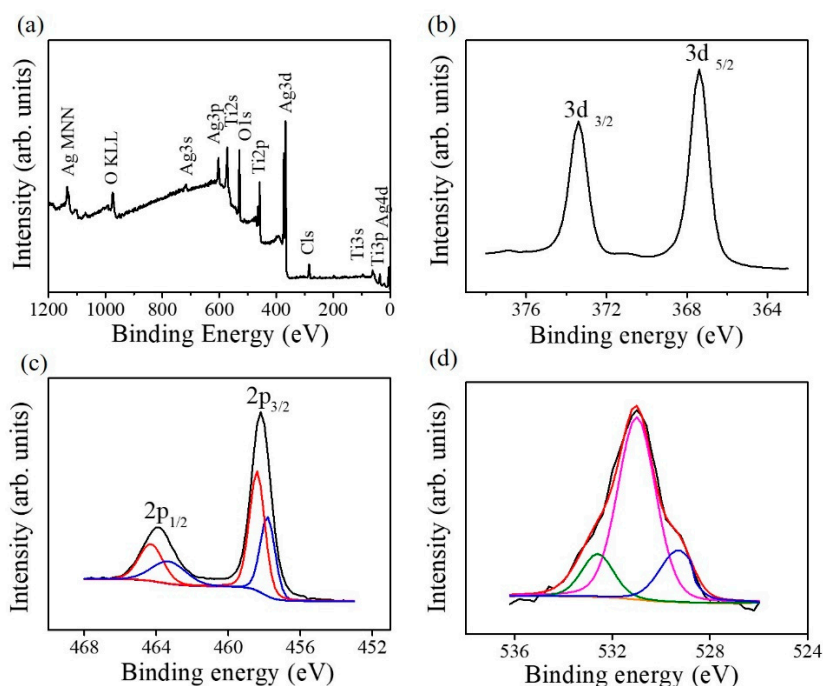


Figure 6. XPS analysis of the $\text{TiO}_2\text{-Ag}_2\text{O-1}$ composite nanorods: (a) Survey scan spectrum. (b) Ag 3d narrow scan spectrum. (c) Ti 2p narrow scan spectrum. The red curve is associated with the contribution of the Ti^{4+} valance state and the blue curve originated from the Ti^{3+} valance state. (d) O1s narrow scan spectrum. The blue and pink curves are ascribed to the lattice oxygen in Ag_2O and TiO_2 , respectively. Moreover, the green curve is ascribed to external absorbed $-\text{OH}$ groups or water molecules on the surfaces of the composite nanorods.

Figure 7 shows the temperature-dependent gas-sensing responses to NO_2 (1.5 ppm) of gas sensors made from TiO_2 , $\text{TiO}_2\text{-Ag}_2\text{O-1}$, and $\text{TiO}_2\text{-Ag}_2\text{O-2}$ composite nanorods. For the NO_2 target gas, the n-type gas-sensing response of nanorod-based sensors is defined as R_g/R_a and the p-type gas-sensing response of nanorod-based sensors is defined as R_a/R_g , where R_g is the sensor resistance under target gas exposure and R_a is the sensor resistance with the removal of the target gas. The optimal operating temperature of oxide sensors to obtain the highest gas-sensing response is highly associated with the balance between the chemical reactions and the gas diffusion rate of the oxide surfaces [5]. The maximum responses of the $\text{TiO}_2\text{-Ag}_2\text{O-1}$ and $\text{TiO}_2\text{-Ag}_2\text{O-2}$ sensors to NO_2 were obtained at the operating temperature of 250 °C in this study. Meanwhile, a relatively high operating temperature of 275 °C was needed for the TiO_2 nanorods to obtain the maximum gas-sensing response under similar gas-sensing test conditions. Notably, the gas-sensing response versus operating temperature curve of $\text{TiO}_2\text{-Ag}_2\text{O-1}$ showed a distinct summit at 250 °C, differing substantially from the curves of the TiO_2 and $\text{TiO}_2\text{-Ag}_2\text{O-2}$ nanorod sensors. This result might be a sign of different gas-detecting mechanisms operating among the various nanorod-based sensors. Therefore, the optimal gas-sensing temperature of the fabricated composite nanorod sensors toward NO_2 was chosen as 250 °C in this study.

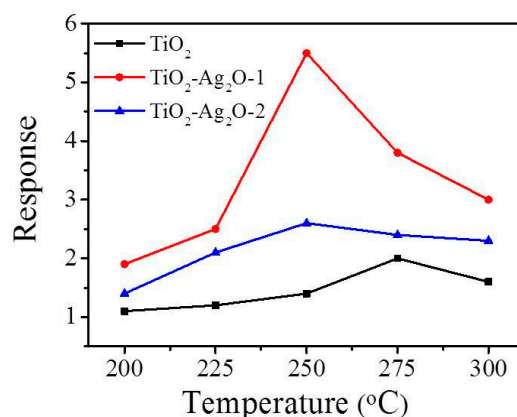


Figure 7. Temperature-dependent gas-sensing responses of various nanorod sensors exposed to 1.5 ppm NO₂.

Figure 8a–c shows the dynamic NO₂ gas-sensing response curves of the TiO₂, TiO₂-Ag₂O-1, and TiO₂-Ag₂O-2 sensors, respectively, upon exposure to 0.5–3.0 ppm NO₂. A sharp increase in sensor resistance was observed for the TiO₂ and TiO₂-Ag₂O-1 nanorod sensors upon exposure to NO₂; moreover, the sensor resistance decreased with the removal of the NO₂ target gas (Figure 8a,b). By contrast, the TiO₂-Ag₂O-2 showed an opposite sensor resistance variation upon exposure to NO₂ gas (Figure 8c). This indicates that the TiO₂ and TiO₂-Ag₂O-1 sensors showed an n-type conduction nature and the TiO₂-Ag₂O-2 sensor demonstrated a p-type conduction nature during the NO₂ gas-sensing tests. The aforementioned structural results reveal that the TiO₂-Ag₂O-1 sensor exhibited a morphology in which the Ag₂O particles were dispersedly distributed on the surfaces of the TiO₂ nanorods. The incomplete coverage of the Ag₂O particles on the TiO₂ surfaces of the TiO₂-Ag₂O-1 nanorods meant that, upon exposure to the NO₂ target gas, the n-type conduction dominated the material's gas-sensing behavior. By contrast, the TiO₂-Ag₂O-2 nanorods demonstrated a thick, full-coverage layer of Ag₂O clusters or aggregations on the surfaces of the TiO₂ nanorods. This morphology feature might account for the conduction and chemoresistive variation in the TiO₂-Ag₂O-2 sensor, which was dominated by p-type Ag₂O shell layers of the composite nanorods. A similar conduction type variation due to the p-type crystal coverage effect on the p–n heterogeneous oxides has been demonstrated in a ZnO–Cr₂O₃ system [11]. Comparatively, the TiO₂-Ag₂O-1 sensor exhibited the largest degree of sensor resistance variation before and after the introduction of the NO₂ gas under the given test conditions. Notably, the pristine TiO₂ sensor demonstrated the lowest sensor resistance variation size upon exposure to NO₂ gas. The plot of NO₂ gas-sensing response versus NO₂ concentration for various TiO₂ nanorod-based sensors is shown in Figure 8d. The NO₂ gas-sensing response of the TiO₂-Ag₂O-1 sensor was approximately 3.1 upon exposure to 0.5 ppm NO₂. Moreover, the gas-sensing response of the TiO₂-Ag₂O-1 sensor increased to 7.6 upon exposure to 3.0 ppm NO₂. An approximate increase of the gas-sensing response by 2.4 times was observed with an increase in NO₂ concentration from 0.5 ppm to 3.0 ppm by the TiO₂-Ag₂O-1 sensor. By contrast, the TiO₂-Ag₂O-2 sensor exhibited gas-sensing responses of approximately 2.2 and 3.1 upon exposure to 0.5 ppm and 3.0 ppm NO₂, respectively; these response values are lower than those of the TiO₂-Ag₂O-1 sensor under similar test conditions. A concentration-dependent increment of the gas-sensing response for a low concentration range of 0.5–3.0 ppm NO₂ was less visible for the TiO₂-Ag₂O-2 sensor. Notably, the gas-sensing response of the pristine TiO₂ sensor at the same operating temperature did not show a response value larger than 2.0, revealing that the decoration of discrete or layered Ag₂O particles or aggregations on the surfaces of TiO₂ nanorods to form a p–n heterogeneous system is beneficial to the enhancement of the NO₂ gas-sensing response of TiO₂ nanorods. The gas-sensing response time of the nanorod-based sensors is defined as the duration required for an occurrence of a 90% change in sensor resistance upon exposure to the target gas, while the recovery time is the duration in which the sensor resistance drops by 90% from the maximal steady-state value, following the removal of the target gas.

The response times for the TiO_2 , $\text{TiO}_2\text{-Ag}_2\text{O-1}$, and $\text{TiO}_2\text{-Ag}_2\text{O-2}$ nanorod sensors upon exposure to 0.5–3.0 ppm NO_2 gas ranged from 85 to 93 s. No substantial difference in the response times of various nanorod sensors exposed to different concentrations of NO_2 gas was observed. By contrast, a marked improvement in the recovery time of the TiO_2 nanorods sputtered with a coating of Ag_2O particles was visibly demonstrated. The recovery times of the pristine TiO_2 nanorod sensor ranged from 405 to 820 s after exposure to 0.5 to 3.0 ppm NO_2 . Decreased recovery times were shown in the $\text{TiO}_2\text{-Ag}_2\text{O-2}$ nanorod sensor, which ranged from 191 to 280 s after exposure to 0.5 to 3.0 ppm NO_2 . Notably, the $\text{TiO}_2\text{-Ag}_2\text{O-1}$ nanorod sensor exhibited a substantial decrease in the recovery time upon the removal of NO_2 gas; the recovery times ranged from 97 to 136 s in the NO_2 concentration range of 0.5 to 3.0 ppm. The size of the Ag_2O particles (or clusters) and their dispersibility are vital factors affecting gas-sensing performance, which lead to the highly effective desorption of surface-adsorbed ions with the removal of the target gas at elevated temperatures [21]. The $\text{TiO}_2\text{-Ag}_2\text{O-1}$ nanorod sensor exhibited the superior gas-sensing performance among the various nanorod sensors in this study. The cycling gas-sensing tests of the $\text{TiO}_2\text{-Ag}_2\text{O-1}$ nanorod sensor exposed to 1.5 ppm NO_2 at 250 °C are shown in Figure 8e. The result indicates that the $\text{TiO}_2\text{-Ag}_2\text{O-1}$ nanorod sensor had good reproducibility during multiple cycles of response and recovery. Figure 8f shows the across selectivity profiles of the $\text{TiO}_2\text{-Ag}_2\text{O-1}$ sensor upon exposure to 100 ppm H_2 , 50 ppm $\text{C}_2\text{H}_5\text{OH}$, and 50 ppm NH_3 gases, as well as 3.0 ppm NO_2 . The $\text{TiO}_2\text{-Ag}_2\text{O-1}$ sensor exhibited a highly selective gas-sensing response toward the low-concentration NO_2 gas as compared to the other various target gases.

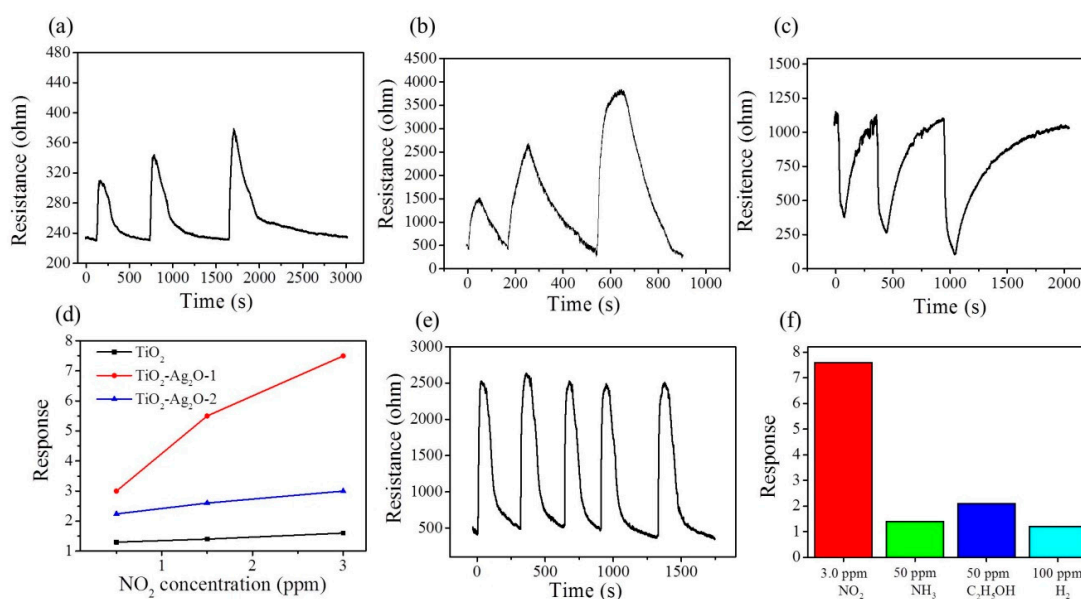


Figure 8. The dynamic response curves of various nanorod sensors to NO_2 gas ranging from 0.5 ppm to 3.0 ppm: (a) TiO_2 , (b) $\text{TiO}_2\text{-Ag}_2\text{O-1}$, and (c) $\text{TiO}_2\text{-Ag}_2\text{O-2}$. (d) Summarized gas-sensing response values versus NO_2 concentration for various nanorod sensors. (e) Cycling gas-sensing tests of $\text{TiO}_2\text{-Ag}_2\text{O-1}$ upon exposure to 1.5 ppm NO_2 at 250 °C. (f) The across selectivity profiles of $\text{TiO}_2\text{-Ag}_2\text{O-1}$ upon exposure to various target gases.

The NO_2 gas-sensing performances of the sensors based on several TiO_2 -based composite oxides are summarized in Table 1. Compared to previous works [22–25], the $\text{TiO}_2\text{-Ag}_2\text{O-1}$ nanorod sensor herein showed superior NO_2 gas-sensing performance under similar test conditions. The gas-sensing test results herein demonstrated that the $\text{TiO}_2\text{-Ag}_2\text{O}$ composite nanorods decorated with discrete Ag_2O particles have potential for applications as NO_2 gas sensors at low concentrations. The possible

surface chemisorption reactions occurring during the gas-sensing process of the TiO₂-Ag₂O composite nanorods upon exposure to NO₂ gas are described below:

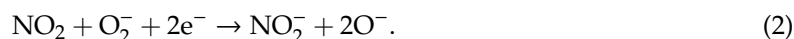


Table 1. NO₂ gas-sensing performance of various TiO₂-based composites prepared using various methods in the operating temperature range of 200–300 °C [22–25].

Composite Nanorods	Synthesis Method	Operating Temperature (°C)	Concentration (ppm)	Response (Ra/Rg)	Detection Limit (ppm)	Response/Recovery Time (s)
TiO ₂ -Ag ₂ O (this work)	Hydrothermal and sputtering method	250	1.5	5.5	0.5	87/112
TiO ₂ -Er ₂ O ₃	Sol-gel method	200	10	4.5	0.5	N/A
TiO ₂ -V ₂ O ₅	Sol-gel and solvothermal method	200	2	0.8	N/A	N/A
TiO ₂ -MoO ₃	Sol-gel method	300	2	2.3	0.5	120/180
TiO ₂ -Ga ₂ O ₃	Sol-gel method	200	2	2.25	N/A	150/270

The NO₂ molecules capture electrons from the oxide surface to form NO₂⁻ ions; this engenders the electron density variation of the oxides. By contrast, the surface-adsorbed NO₂⁻ ions are desorbed with the removal of the NO₂ gas and, consequently, in this process the recovery of the initial conditions takes place. Notably, the contact of the TiO₂-Ag₂O oxides form p-n junctions at the hetero-interfacial regions. This additionally formed potential barrier in the TiO₂-Ag₂O composite nanorods explains the superior gas-sensing responses of the composite nanorods compared to that of the pristine TiO₂ nanorods. A similar formation of heterogeneous p-n junctions improves the gas-sensing responses of composite nanorods, as has been demonstrated in ZnO-ZnCr₂O₄, ZnO-Mn₃O₄, and ZnO-Cr₂O₃ p-n composite structures [9–11]. Furthermore, the reasons for the NO₂ gas-sensing response of the TiO₂-Ag₂O-1 sensor being higher than that of the TiO₂-Ag₂O-2 sensor at the given test conditions are explained by the schematic mechanisms exhibited in Figure 9. The schematic of the gas sensor device is also shown in Figure 9a. When the Ag₂O particles are coated on the surfaces of the TiO₂ nanorods in a discrete configuration, the randomly distribution of the depletion region at the interface of the p-Ag₂O and n-type TiO₂ will initially narrow the space of the conducting channel along the radial direction of the TiO₂ (Figure 9a). Moreover, the exposure of the free surfaces of the Ag₂O particles and TiO₂ rods in ambient air also initially lead to a surface hole accumulation layer and depletion layer, respectively. Furthermore, following the decoration of the Ag₂O particles in a continuous layer configuration on the surfaces of the TiO₂ nanorods, the conducting channel in the TiO₂ will also be narrowed (Figure 9b). After introducing NO₂ gas into the test chamber, the depletion region size at the TiO₂-Ag₂O hetero-interfacial region of the TiO₂-Ag₂O-1 sensor varies due to the surface-adsorbed NO₂⁻ ions. Moreover, the surface depletion region of the TiO₂ nanorods is also thickened. The variation of the depletion size at different regions, further narrowing the conduction channel size of the TiO₂ nanorods, results in the increased sensor resistance of the TiO₂-Ag₂O-1 nanorod sensor. By contrast, the TiO₂-Ag₂O-2 nanorod sensor exhibits a p-type conduction gas-sensing behavior in this study. This reveals that the conduction channel size in the TiO₂ nanorod of the composite nanorod no longer plays a vital role affecting the chemoresistive variation upon exposure to NO₂ gas. It has also been shown that in core-shell ZnO-ZnMn₂O₄ and ZnO-Cr₂O₃ nanostructures, the p-n contact regions at the hetero-interfaces no longer play significant roles in the gas-sensing reaction [10,11]. The conduction path in the Ag₂O layer, by contrast, dominates the gas-sensing response of the TiO₂-Ag₂O-2 nanorod sensor. Notably, when the TiO₂-Ag₂O-2 nanorod is exposed to NO₂ gas, the accumulation layer in the Ag₂O layer thickens. This increases the carrier number in the p-type Ag₂O layer; therefore, a decreased sensor resistance is expected. However, the surface Ag₂O layer-dominated chemoresistive variation size of the TiO₂-Ag₂O-2 nanorod sensor is expected to be lower than that of the TiO₂-Ag₂O-1

nanorod sensor, which is dominated by the rugged conduction channel size in the TiO_2 core region upon exposure to NO_2 gas. Therefore, the superior NO_2 gas-sensing performance was obtained by the TiO_2 - Ag_2O -1 nanorod sensor in this study.

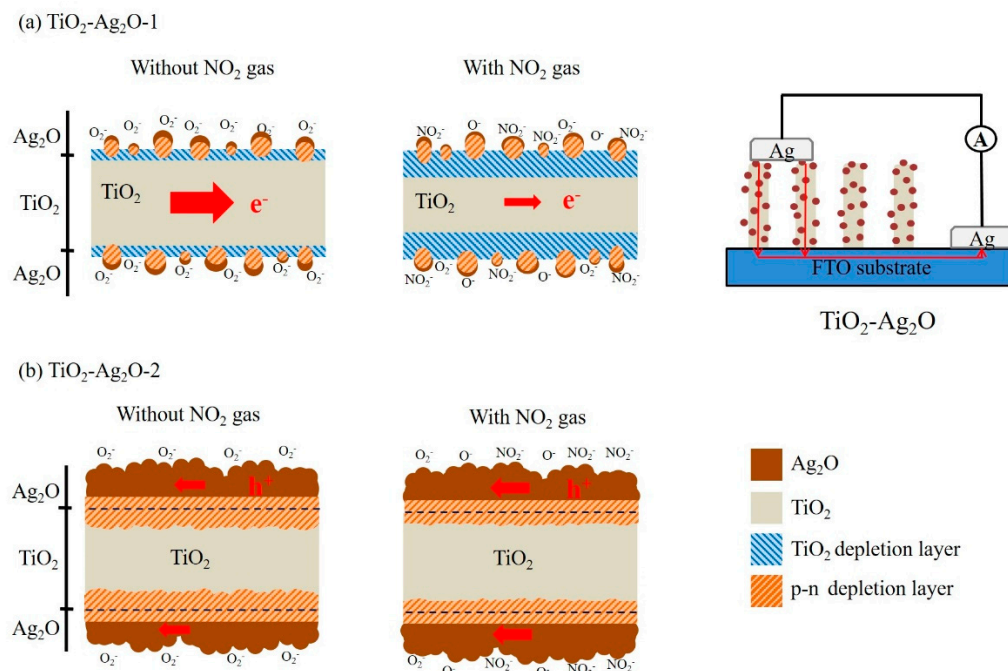


Figure 9. Schematic illustrations for possible gas-sensing mechanisms of (a) TiO_2 - Ag_2O -1 and (b) TiO_2 - Ag_2O -2 toward NO_2 gas.

4. Conclusions

In summary, TiO_2 - Ag_2O composite nanorods were synthesized through the combination of hydrothermal growth and sputtering methods. The structural analysis reveals that the as-synthesized TiO_2 - Ag_2O composite nanorods have a high crystallinity. The electron microscopy analysis results demonstrate that a shorter Ag_2O sputtering duration causes the formation of TiO_2 - Ag_2O composite nanorods decorated with discrete Ag_2O particles. Meanwhile, a prolonged Ag_2O sputtering process engenders the aggregation of numerous Ag_2O particles, which form a layered configuration on the composite nanorods. The formation of p-n junctions in the composite nanorods enhances their NO_2 gas-sensing performance as compared to pristine TiO_2 nanorods. Moreover, different gas-sensing mechanisms of the TiO_2 - Ag_2O nanorods with various Ag_2O coverage morphologies account for the superior NO_2 gas-sensing responses of the TiO_2 - Ag_2O -1 sensor at a low concentration range in this study.

Author Contributions: Methodology, Y.-C.L. (Yen-Chen Liu); formal analysis, Y.-C.L. (Yen-Chen Liu); writing—original draft preparation, Y.-C.L. (Yuan-Chang Liang); supervision, Y.-C.L. (Yuan-Chang Liang).

Funding: This research was funded by the Ministry of Science and Technology of Taiwan. Grant No. MOST 105-2628-E-019-001-MY3 and MOST 108-2221-E-019-034-MY3.

Conflicts of Interest: The authors declare no conflict of interest.

References

1. Liang, Y.C.; Chao, Y. Crystal phase content-dependent functionality of dual phase SnO_2 - WO_3 nanocomposite films via cosputtering crystal growth. *RSC Adv.* **2019**, *9*, 6482–6493. [[CrossRef](#)]
2. Liang, Y.C.; Lee, C.M.; Loa, Y.J. Reducing gas-sensing performance of Ce-doped SnO_2 thin films through a cosputtering method. *RSC Adv.* **2017**, *7*, 4724–4734. [[CrossRef](#)]

3. Liang, Y.C.; Chao, Y. Enhancement of Acetone Gas-Sensing Responses of Tapered WO₃ Nanorods through Sputtering Coating with a Thin SnO₂ Coverage Layer. *Nanomaterials* **2019**, *9*, 864. [[CrossRef](#)] [[PubMed](#)]
4. Liang, Y.C.; Chang, C.W. Improvement of Ethanol Gas-Sensing Responses of ZnO–WO₃ Composite Nanorods through Annealing Induced Local Phase Transformation. *Nanomaterials* **2019**, *9*, 669. [[CrossRef](#)] [[PubMed](#)]
5. Liang, Y.C.; Xu, N.C.; Wang, C.C.; Wei, D.H. Fabrication of Nanosized Island-Like CdO Crystallites-Decorated TiO₂ Rod Nanocomposites via a Combinational Methodology and Their Low-Concentration NO₂ Gas-Sensing Behavior. *Materials* **2017**, *10*, 778. [[CrossRef](#)] [[PubMed](#)]
6. Zhao, Y.P.; Li, Y.H.; Ren, X.P.; Gao, F.; Zhao, H. The Effect of Eu Doping on Microstructure, Morphology and Methanal-Sensing Performance of Highly Ordered SnO₂ Nanorods Array. *Nanomaterials* **2017**, *7*, 410. [[CrossRef](#)]
7. Liang, Y.C.; Xu, N.C. Synthesis of TiO₂–ZnS nanocomposites via sacrificial template sulfidation and their ethanol gas-sensing performance. *RSC Adv.* **2018**, *8*, 22437–22446. [[CrossRef](#)]
8. Liang, Y.C.; Wang, C.C. Hydrothermally derived zinc sulfide sphere-decorated titanium dioxide flower-like composites and their enhanced ethanol gas-sensing performance. *J. Alloys Compound.* **2018**, *730*, 333–341. [[CrossRef](#)]
9. Liang, Y.C.; Hsia, H.Y.; Cheng, Y.R.; Lee, C.M.; Liu, S.L.; Lina, T.Y.; Chung, C.C. Crystalline quality-dependent gas detection behaviors of zinc oxide–zinc chromite p–n heterostructures. *CrystEngComm* **2015**, *17*, 4190–4199. [[CrossRef](#)]
10. Na, C.W.; Park, S.Y.; Chung, J.H.; Lee, J.H. Transformation of ZnO Nanobelts into Single-Crystalline Mn₃O₄ Nanowires. *ACS Appl. Mater. Interfaces* **2012**, *4*, 6565–6572. [[CrossRef](#)]
11. Woo, H.S.; Na, C.W.; Kim, D.; Lee, J.H. Highly sensitive and selective trimethylamine sensor using one-dimensional ZnO–Cr₂O₃ hetero-nanostructures. *Nanotechnology* **2012**, *23*, 245501. [[CrossRef](#)]
12. Suna, G.; Chen, H.L.; Li, Y.W.; Chen, Z.H.; Zhang, S.S.; Ma, G.Z.; Jia, T.K.; Cao, J.L.; Bala, H.; Wang, X.D.; et al. Synthesis and improved gas sensing properties of NiO-decorated SnO₂ microflowers assembled with porous nanorods. *Sens. Actuators B* **2016**, *233*, 180–192. [[CrossRef](#)]
13. Kim, H.W.; Na, H.G.; Kwak, D.S.; Cho, H.Y.; Kwon, Y.J. Enhanced Gas Sensing Characteristics of Ag₂O-Functionalized Networked In₂O₃ Nanowires. *Jpn. J. Appl. Phys.* **2013**, *52*, 10MD01. [[CrossRef](#)]
14. Rajabi, A.; Ghazali, M.J.; Mahmoudi, E.; Baghdadi, A.H.; Mohammad, A.W.; Mustafah, N.M.; Ohnmar, H.; Naicker, S.A. Synthesis, Characterization, and Antibacterial Activity of Ag₂O-Loaded Polyethylene Terephthalate Fabric via Ultrasonic Method. *Nanomaterials* **2019**, *9*, 450. [[CrossRef](#)] [[PubMed](#)]
15. Ma, S.S.; Xue, J.J.; Zhou, Y.; Zhang, Z. Photochemical synthesis of ZnO–Ag₂O heterostructures with enhanced ultraviolet and visible photocatalytic activity. *J. Mater. Chem. A.* **2014**, *2*, 7272–7280. [[CrossRef](#)]
16. Li, C.; Hsieh, J.H.; Cheng, J.C.; Huang, C.C. Optical and photoelectrochemical studies on Ag₂O/TiO₂ double-layer thin films. *Thin Solid Films* **2014**, *570*, 436–444. [[CrossRef](#)]
17. Sarkar, D.B.; Ghosh, C.K.; Mukherjee, S.; Chattopadhyay, K.K. Three Dimensional Ag₂O/TiO₂ Type-II (p–n) Nanoheterojunctions for Superior Photocatalytic Activity. *ACS Appl. Mater. Interfaces* **2013**, *5*, 331–337. [[CrossRef](#)]
18. Kaushik, V.K. XPS core level spectra and Auger parameters for some silver compounds. *J. Electron Spectrosc. Relat. Phenom.* **1991**, *56*, 273. [[CrossRef](#)]
19. Ingo, G.M.; Dirè, S.; Babonneau, F. XPS studies of SiO₂-TiO₂ powders prepared by sol-gel process. *Appl. Surf. Sci.* **1993**, *70*, 230–234. [[CrossRef](#)]
20. Wei, N.; Cui, H.Z.; Song, Q.; Zhang, L.; Song, X.J.; Wang, K.; Zhang, Y.F.; Li, J.; Wen, J.; Tian, J. Ag₂O nanoparticle/TiO₂ nanobelt heterostructures with remarkable photo-response and photocatalytic properties under UV, visible and near-infrared irradiation. *Appl. Catal. B* **2016**, *198*, 83–90. [[CrossRef](#)]
21. Yang, T.L.; Yang, Q.Y.; Xiao, Y.; Sun, P.; Wang, Z.; Gao, Y.; Ma, J.; Sun, Y.F.; Lu, G.Y. A pulse-driven sensor based on ordered mesoporous Ag₂O–SnO₂ with improved H₂S-sensing performance. *Sens. Actuators B* **2016**, *228*, 529–538. [[CrossRef](#)]
22. Mohammadi, M.R.; Fray, D.J. Development of nanocrystalline TiO₂–Er₂O₃ and TiO₂–Ta₂O₅ thin film gas sensors: Controlling the physical and sensing properties. *Sens. Actuators B* **2009**, *141*, 76–84. [[CrossRef](#)]
23. Epifani, M.R.; Comini, E.B.; Díaz, R.; Force, C.; Siciliano, P.T.; Faglia, G.D. TiO₂ colloidal nanocrystals surface modification by V₂O₅ species: Investigation by ⁴⁷Ti MAS-NMR and H₂, CO and NO₂ sensing properties. *Appl. Surf. Sci.* **2015**, *351*, 1169–1173. [[CrossRef](#)]

24. Galatsis, K.; Li, Y.X.; Wlodarski, W.; Comini, E.; Faglia, G.; Sberveglieri, G. Semiconductor MoO₃-TiO₂ thin film gas sensors. *Sens. Actuators B* **2001**, *77*, 472–477. [[CrossRef](#)]
25. Mohammadi, M.R.; Fray, D.J. Semiconductor TiO₂-Ga₂O₃ thin film gas sensors derived from particulate sol-gel route. *Acta Mater.* **2007**, *55*, 4455–4466. [[CrossRef](#)]



© 2019 by the authors. Licensee MDPI, Basel, Switzerland. This article is an open access article distributed under the terms and conditions of the Creative Commons Attribution (CC BY) license (<http://creativecommons.org/licenses/by/4.0/>).